5-2010

Partial phonon density of states of 57-iron and 161-dysprosium in DyFe3 by nuclear resonant inelastic X-ray scattering under high pressure

Elizabeth Anne Tanis
University of Nevada Las Vegas

Repository Citation

PHONON DENSITY OF STATES OF 57-IRON AND 161-DYSPROSIUM IN

DyFe$_3$ BY NUCLEAR RESONANT INELASTIC X-RAY SCATTERING

UNDER HIGH PRESSURE

by

Elizabeth Anne Tanis

Bachelor of Science
California Lutheran University
2006

A thesis submitted in partial fulfillment
of the requirements for the

Master of Science Degree in Physics
Department of Physics
College of Sciences

Graduate College
University of Nevada, Las Vegas
May 2010

THE GRADUATE COLLEGE

We recommend the thesis prepared under our supervision by

Elizabeth Anne Tanis

entitled

Partial Phonon Density of States of 57-Iron and 161-Dysprosium in DyFe$_3$ by Nuclear Resonant Inelastic X-Ray Scattering Under High Pressure

be accepted in partial fulfillment of the requirements for the degree of

Master of Science Physics
Physics and Astronomy

Lon Spight, Committee Chair

Dave Schiferl, Committee Co-chair

Pamela Burnley, Committee Member

Len Zane, Committee Member

Adam Simon, Graduate Faculty Representative

Ronald Smith, Ph. D., Vice President for Research and Graduate Studies
and Dean of the Graduate College

May 2010

ABSTRACT

Phonon Density of States of 57-Iron and 161-Dysprosium in DyFe$_3$ By Nuclear Resonant Inelastic X-Ray Scattering Under Pressure

by

Elizabeth Anne Tanis

Dr. Lon Spight, Examination Committee Chair
Professor of Physics
University of Nevada, Las Vegas

The dual partial phonon density of states (DOS) from two different Mössbauer isotopes (^{161}Dy and ^{57}Fe) in the same material (dyfe$_3$) was successfully measured using the nuclear resonant inelastic x-ray scattering (NRIXS) technique at high pressure. Nuclear inelastic scattering measurements yield an in-depth understanding of the element-specific dynamic properties. The Debye temperatures (Θ_D), the Lamb-Mössbauer factor (f_{LM}), and the vibrational contributions to the Helmholtz free energy (F_{vib}), specific heat (c_V), entropy (S_{vib}) and internal energy (U_{vib}) are calculated directly from the phonon density of states.

TABLE OF CONTENTS

LIST OF FIGURES

ACKNOWLEDGMENTS

In memory of
Dr. Malcolm F. Nicol

CHAPTER 1

INTRODUCTION

Lattice dynamics are important in understanding various phenomena and properties of solids such as thermodynamic properties, phase transitions and soft modes. Determination of the lattice dynamics of inter-metallic compounds at high pressure representes a major experimental challenge and that has eluded previous attempts. By using the nuclear inelastic scattering technique, access to the partial density of vibrational states of a specific atom can be found, however that atom must have a Mössbauer active nuclide. The partial phonon density of states (PDOS) gives deeper insight to lattice dynamics at high pressure; which is of great importance and interest in the material and geoscience communities. Measurements of the PDOS also present an opportunity to test the accuracy of theoretical calculations of the total DOS from one isotope. This thesis discusses the successful measurement of the phonon density of states (DOS) from two different Mössbauer isotopes (^{161}Dy and ^{57}Fe) in the same material (DyFe$_3$) using the nuclear resonant inelastic x-ray scattering (NRIXS) technique at high pressure.

Iron is the most abundant element in the dense metal cores of planets, such as Earth and also in many meteorites. Iron and iron alloys are also the most common source of ferromagnetic materials in everyday use. Iron is the most common Mössbauer isotope used in NRIXS experiments. Dysprosium, in contrast, has only been measured via NRIXS a few times. Due to its large absorption and high excitation energy, previous attempts to measure the pure ^{161}Dy DOS at ambient conditions and at low temperature have been made but there has been no recently published data for ^{161}Dy at high pressure [1, 2, 3].

Only a few studies using NRIXS have been conducted to investigate the dual partial phonon density of states. The partial phonon DOS for each Mössbauer isotope in EuFe$_4$Sb$_{12}$ and DyFe$_2$ have been successfully studied at ambient conditions [2, 4].

dyfe$_3$ is of particular interest for several reasons. First, we have the ability to synthesize the material at UNLV with enriched [57]Fe and [161]Dy. Dy has similar characteristics to other lanthanides for which we currently do not have the capability to experiment on. Second, DyFe$_3$ is a less complex sample, which enables theorists to test and enhance their models for future more complex samples.

Nuclear inelastic scattering measurements yield an in-depth understanding of the element-specific dynamic properties. Lattice vibrations are the dominant contributor to the entropy as well as to the thermal pressure in solids, and thus figure very prominently in the study of high-pressure phase stability and equation of state. It is also possible to determine the sound velocity of the sample, as well as the Debye temperatures, the Lamb-Mössbauer factor, (more accurately than with the Mössbauer effect), and the vibrational contributions to the Helmholtz free energy, specific heat, entropy and internal energy from the phonon density of states [5, 6].

Properties of DyFe$_3$

The inter-metallic compound, DyFe$_3$, is composed of the 3d transition metal Fe and the rare earth element Dy. Numerous structure studies using x-ray diffraction show that DyFe$_3$ has a rhomohedral structure. It is in the space group, R$\bar{3}$m, number 166 [7, 8, 9, 10, 11]. The Fe atoms occupy the 3b site (0, 0, $\frac{1}{2}$), the 6c site (0, 0, 0.334), and the 18h site ($\frac{1}{2}$, $\frac{1}{2}$, 0.083). The Dy atoms occupy the 3a site (0, 0, 0) and 6c site (0, 0, 0.141) [12]. There are 3 atoms in the primitive cell. The structure is shown in figure 1. The unit cell parameters of DyFe$_3$ are: a = 5.122(1) and c = 24.57(1) [13]. The theoretical density of DyFe$_3$ is 8.836 g/cm^3.

DyFe$_3$ has been measured at ambient pressure with a variety of techniques to study many different properties. Extensive Mössbauer experiments have been preformed, as well as neutron diffraction, and other magnetization measurements. The Curie temperature, T$_C$, of DyFe$_3$ is between 600 and 616 K. DyFe$_3$ melts congruently at 1573 K.

The Dy moments couple ferromagnetically to each other but anti-ferromagnetically with the Fe moments. At low temperature, Fe moments dominate the magnetic moments. At higher temperatures the Fe moments get weaker and at the compensation point (T_{comp}, between 521 and 560 K) the moments of the Fe are the same as the moments from the Dy. It appears as if the sample is non-magnetic due to the moments coupling anti-ferromagnetically to each other [14, 15, 16, 17, 18, 19, 20, 21, 22, 23].
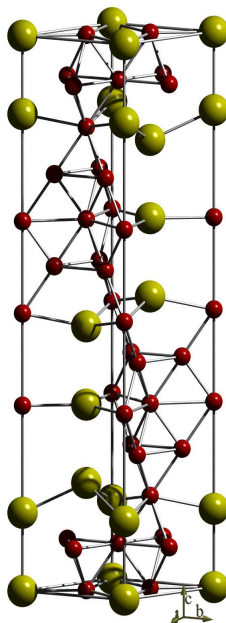
Figure 1 DyFe$_3$ rhomohedral structure. The Fe atoms occupy the 3b site $(0, 0, \frac{1}{2})$, the 6c site $(0, 0, 0.334)$, and the 18h site $(\frac{1}{2}, \frac{1}{2}, 0.083)$. The Dy atoms occupy the 3a site $(0, 0, 0)$ and 6c site $(0, 0, 0.141)$ [12, 13].

High Pressure Techniques

High pressure research enables a better understanding of the structural properties of materials, chemical reaction and of material synthesis.

The reliable and controlled replication of high pressure in the laboratory begins

with the fundamental equation for pressure: $p = F/A$ where p is the pressure, F, the applied force, and A, the area. The operation of the diamond anvil cell relies on this fundamental principle. High pressure can be achieved by applying a moderate force on a sample with a small area, rather than applying a large force on a large area.

Over the course of more than two decades, commencing in 1958, the diamond anvil cell (DAC) developed from a rather crude qualitative instrument to the sophisticated quantitative research tool it is today, capable of routinely producing sustained static pressures in the multi-megabar range and readily adaptable to numerous scientific measurement techniques because of its optical accessibility, miniature size, and portability.

Diamond anvil cells were independently invented by two groups: National Bureau of Standards (NBS, now the National Institute of Standards and Technology, NIST) and University of Chicago. Both groups made use of two opposed diamonds in a Bridgman flat-face anvil arrangement, shown in figure 2 [24, 25]. The only limitation imposed by the use of pressure is the failure or limit of the pressure producing vessel itself. The scientists knew that diamond, because of its extreme hardness, high compressive strength and transmission properties, was the obvious material to use for the anvils. High pressure is only limited by the deformation and fracture of the diamonds under very high loads. At this time the sample was simply placed between the anvils and the anvils were driven together by a lever arm. Only powder samples could be investigated and pressure was crudely determined by calculating force per unit area or by x-ray powder diffraction experiments, which were tedious and time consuming. This created a demand for developing techniques for studying 1) other samples, such as liquids and single crystals and 2) rapid, convenient and accurate pressure determination.

In 1962, Alvin Van Valkenburgh, from NBS, had the ingenious idea of encapsulating pure liquid samples in the DAC by using a thin metal gasket (figure 2) containing

a very small hole placed between the flat surfaces of the opposed anvils. The hole was filled with liquid and the anvils were squeezed together. The metal foil thinned down reducing the volume of the hole and the confining the liquid, thereby increasing the pressure. At about 0.98 GPa, he found that water crystallized to ice [26, 27]. Valkenburgh further employed this gasket technique on single crystals using the liquid as a pressure-transmitting medium [28]. The development of the gasket technique was very important for it permitted hydrostatic pressure environments to be achieved by reducing and even eliminating pressure gradients in the sample.

By 1971, the DAC had undergone several stages of refinement; however the difficulty in measuring the sample pressure adequately still remained. While having a casual lunch together, the scientist at NBS were discussing the problem of measuring pressure in the DAC. When a pivotal question was asked, "Have you considered fluorescence spectroscopy?" Among the many possible techniques NBS had tested and found to be unsuitable, fluorescence was not one of them [27]. Ruby (Al_2O_3) revealed to be the most promising pressure sensor because its intense fluorescence lines (the R_1 and R_2 doublet) are sharp and show a shift with pressure [29, 30]. The very small ruby crystal can be present in the sample chamber to detect pressures without interfering with any other specimen under investigation in the chamber, including the pressure-transmitting liquid itself.

One difficulty with the ruby fluorescence method, is that the R_1 and R_2 lines broaden due to inhomogeneous stresses in the pressure-transmitting medium surrounding the ruby therfore pressure measurements become inaccurate. This consequence resulted in two major advancements of DAC techniques: Extensive research on various hydrostatic pressure transmitting mediums, and further calibration of the ruby pressure sensor, both of which are still being done today [31]. These advancements have contributed to the diamond anvil cell becoming the premier instrument of choice for conducting many kinds of experiments in many disciplines that utilize

5

static high pressure and temperature variables.

Force

Diamond

Gasket

Ruby

Sample

Force
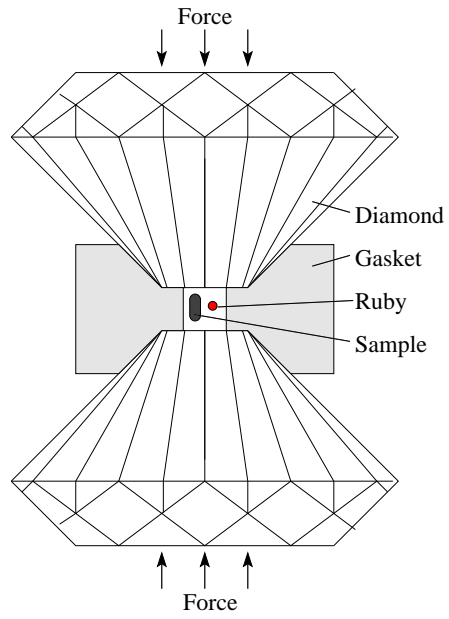
Figure 2 The Bridgman anvil arrangement and schematic of a diamond anvil cell.

CHAPTER 2

THE BASICS OF LATTICE DYNAMICS

In a solid, atoms are firmly bound in a crystalline structure at specific lattice points. These atoms can execute small vibrations around their equilibrium position. As a consequence, the displacement from one atom will cause movement in the surrounding atoms. This type of vibrational motion propagates through the entire solid producing a wave motion, *i.e.* lattice wave [32, 33].

Reciprocal Lattice and Brillouin Zones

In crystallography, the reciprocal lattice is the frequency-space Fourier transform of the direct lattice. Where the reciprocal lattice vectors (a*, b*, c*) are defined to be perpendicular to two of the three real space lattice vectors (a, b, c). The distance from each point to the origin is inversely proportional to spacing of the specific lattice planes. The relationships are described below.

$$a^* = 2\pi \frac{b \times c}{|a \cdot (b \times c)|}$$
$$b^* = 2\pi \frac{c \times a}{|a \cdot (b \times c)|} \qquad (2.1)$$
$$c^* = 2\pi \frac{a \times b}{|a \cdot (b \times c)|}$$

The first Brillouin zone is a uniquely defined primitive cell of the reciprocal lattice. Values of the wave vector outside the first Brillouin zone reproduce the lattice motions described inside the Brillouin zone. Thus, only in the first Brillouin zone is the range of the wave vector physically significant. As an example, the transformation from (a) real space to (b) reciprocal space and (c) the Brillouin zone for a body centered cubic (bcc) lattice is shown in figure 3.

(a) Bravis Lattice (bcc)
Real Space

(b) Reciprocal Lattice (fcc)
k Space
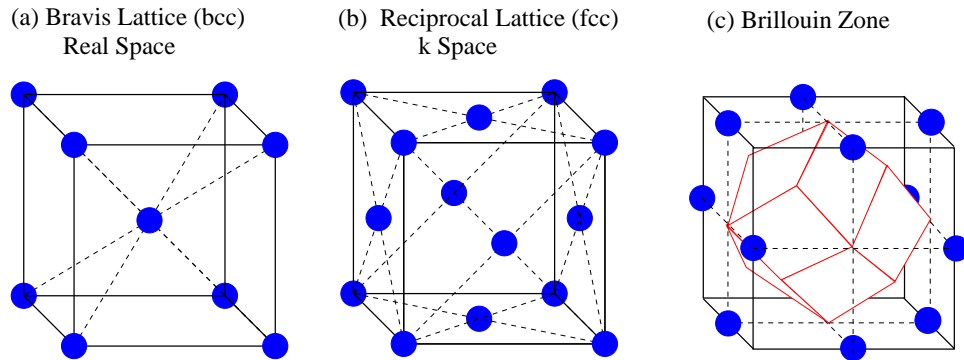
(c) Brillouin Zone

Figure 3 The transformation from (a) the real space body centered cubic (bcc) lattice to (b) the reciprocal space face centered cubic (fcc) lattice and finally (c) the Brillouin zone in red.

Waves and Branches

When a wave propagates along a specific direction, K, considered the wave vector, entire planes of atoms will move in phase with their displacements either parallel or perpendicular to the direction of the wave vector. For each wave vector there are three wave modes: one longitudinal wave, in which the wave propagates along the direction of atomic vibration and two transverse waves in which the wave propagates in directions perpendicular to atomic vibration.

If the atoms vibrate opposite of each other but their center of mass is fixed then the motion is a high frequency mode called an optical vibration (a and b of figure 4). This motion can be excited with a light wave hence the name "optical" branch. If the center of mass of the atoms moves together, as in the long wavelength of acoustical vibrations, it is a low frequency mode considered an "acoustical" vibration (c and d of figure 4).
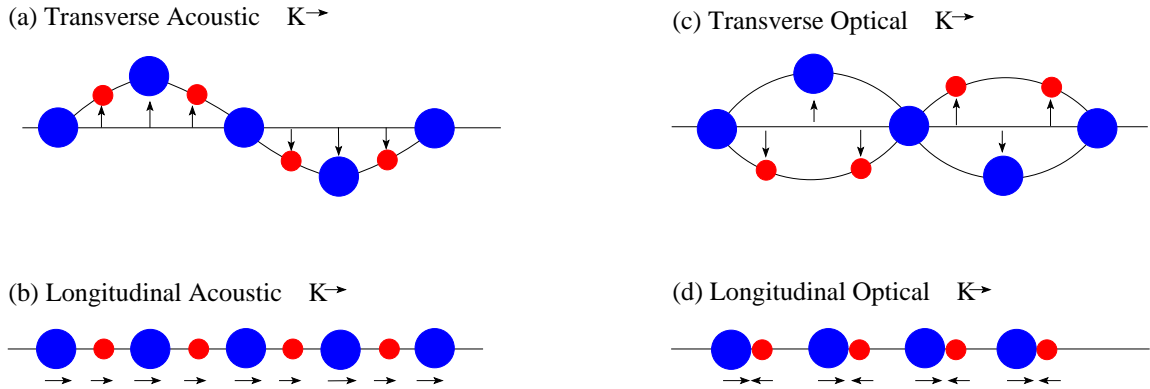
Figure 4 Acoustic (a) transverse, (b) longitudinal motion: the atoms move together. Optical (c) transverse (d) longitudinal motion: the atoms move against each other.

For each mode in a specific direction, a relationship between the frequency, ω, and wave vector, K, is created; called a dispersion curve or dispersion relation. The dispersion relation can provide new information about crystals with two or more atoms per unit/primitive cell. Each dispersion relation develops two branches, the acoustic and the optical branch. For each branch there are three modes corresponding to one longitudinal and two transverse waves. Thus, if there are p atoms in the primitive cell, there are $3p$ branches to the dispersion relation: 3 acoustical and $3p$-3 optical. The longitudinal acoustic phonons give the longitudinal sound velocity, and the transverse acoustic phonons give the transverse sound velocity. The dispersion curves for a Debye solid are shown in figure 5, part a. The theoretically calculated dispersion curves corresponding to an experimental DOS for Sn is shown in figure 6, part a [34].

Quantization of Vibrations: The Phonons

As the atoms participate in the vibrations, the energy quanta of their collective motion are the phonons. Phonons are analogous to the photon of electromagnetic

waves. Phonons are classified as quasi-particles because they have no mass and their wavelength is usually very long, therefore it is a non-localized state. A single phonon "occupies" a particular mode when the corresponding wave has the minimum amplitude. The addition of a second phonon to the state simply increases the amplitude but leaves the wave vector and frequency unaffected. Each lattice wave or each type of vibration produces one type of phonon, therefore $n=1$, 2, or 3 *ect.* is the number of phonons with frequency, ω. They are all identical particles with zero spin (bosons). The minimum energy exchanged between a photon and the lattice is one phonon. The higher the temperature is, the larger the amplitudes of lattice waves, and consequently the higher the average energy and the higher the average number of phonons [35].

The Density of States

The phonon density of states correspond to the frequency distribution of the various types of lattice vibrations from one symmetry point to another in the Brillouin zone.

The Einstein model and the Debye model have been widely used for calculating phonon density of states. In the Einstein model, each atom vibrates like a simple harmonic oscillator. All the atoms are vibrating independently with the same frequency. The excitation spectrum of the crystal consists of levels spaced a distance, hv apart, where v is the Einstein frequency: the frequency of oscillation of each atom in it's potential well. This model is a good approximation for an optical branch however it is over simplified. In a real crystal, interactions between atoms are strong enough that they will inevitably affect their neighbors [35].

The Debye model assumes that the lattice waves are elastic waves (one longitudinal and two transverse, as in figure 5). The frequency is not a constant but has a specific distribution with a cutoff frequency, ω_D, above which no phonons are excited. In the

Debye model, $g(\omega)$ takes the following form (equation 2.2), where ω_D is a parameter, not the actual maximum phonon frequency in the solid.

$$g(\omega) = \begin{cases} 3\omega^2/\omega_D^3, & \text{when } \omega < \omega_D \\ 0, & \text{when } \omega > \omega_D \end{cases} \tag{2.2}$$

For an ideal Debye solid, the Debye-temperature, $\Theta_D(n) = \Theta_D$ for all n-phonon values. For a real solid, $\Theta_D(n)$ depends on n, which gives a measure of the difference between the actual phonon spectra and the Debye spectrum. An example of the Deybe model compared to a typical experimental DOS is shown in figure 5. The Debye model is the most successful in describing the vibrational frequency distribution, $g(E)$ despite large deviations from the experimental $g(E)$ [35].
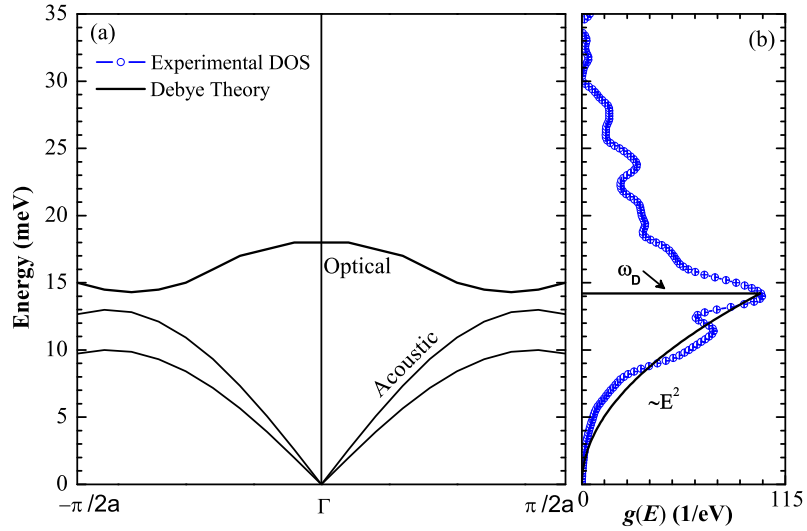
Figure 5 (a) Optical and acoustic branches for a Debye solid. (b) Example of a Debye approximation curve and actual DOS.
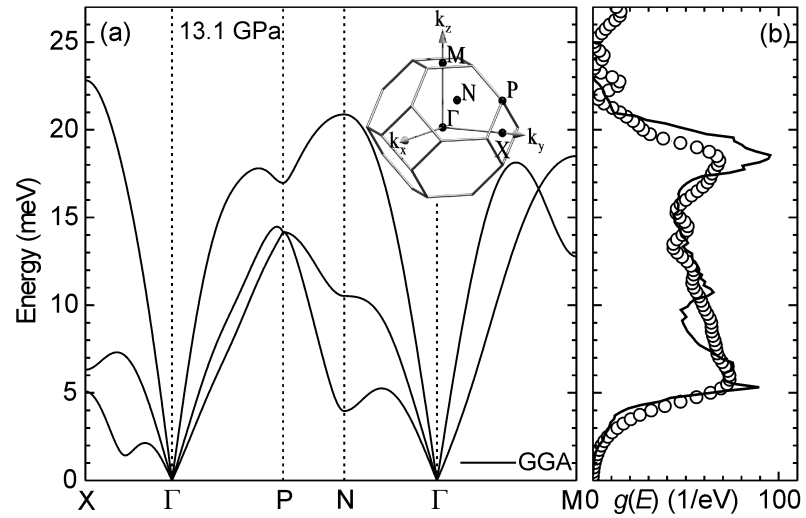
Figure 6 (a) Theoretically calculated dispersion curves and (b) the calculated and experimental DOS for Sn [34]. The Sn is at 13 GPa and 300 K. It has a body center tetragonal (bct) structure with two atoms in the unit cell [36]. The Brillouin zone is in the inset.

CHAPTER 3

NUCLEAR RESONANT SCATTERING

The ^{57}Fe and ^{161}Dy Nucleus

A nucleus that is excited by resonance absorption of x-rays may decay via one of two mechanisms: radioactive decay or by internal conversion with subsequent fluorescence. The process of internal conversion consists of a direct transfer of energy through the electromagnetic interaction between the nucleus in an excited state and one of the electrons of the atom. The nucleus decays to a lower state, without ever producing a γ-ray. The relative probabilities of the two mechanism are $1/(1+\alpha)$ and $\alpha/(1+\alpha)$, respectively. Where α is the internal conversion coefficient. For Mössbauer isotopes, $\alpha > 1$ and therefore internal conversion is the dominating mechanism for decay [35].

The nucleus decays into the ground state by transferring the excitation energy to the electron shell. After the electron is expelled, the hole is quickly filled by other electrons with the emission of fluorescence x-rays. These decay products are emitted with a delay relative to the time of excitation of the nucleus, and the average delay time is given by the natural lifetime, τ of the element. The decay and nuclear scheme of the ^{161}Dy and ^{57}Fe nucleus is shown in figure 7.

The de-excitation of a ^{57}Fe nucleus *via* the internal conversion channel results in the emission of atomic fluorescence radiation with relatively low energies K$_\alpha$ $\sim$6.4 keV and K$_\beta$ $\sim$7 keV with K$_\alpha$ being the most probable channel. Similar to the case of the ^{57}Fe isotope, the de-excitation of a ^{161}Dy nucleus *via* the L shell also results in relatively low energies where L$_\alpha$ $\sim$ 6.5 keV, L$_\beta$ $\sim$7.2 and 7.6 keV, and L$_\gamma$ $\sim$ 8.4keV with L$_\alpha$ being the most probable channel.

The lifetime of an excited state is frequently described in terms of its width. According to the energy-time uncertainty principle, if an average nucleus survives in

an excited state for the lifetime τ of the state, then its energy in the state can be specified within an energy range Γ, satisfying the relation $\Gamma = \hbar/\tau$. Excited states are therefore spread over an energy range of width, Γ [37]. The relatively long lifetimes of Mössbauer isotopes, specifically ^{57}Fe and ^{161}Dy, make them ideal candidates for NRIXS.
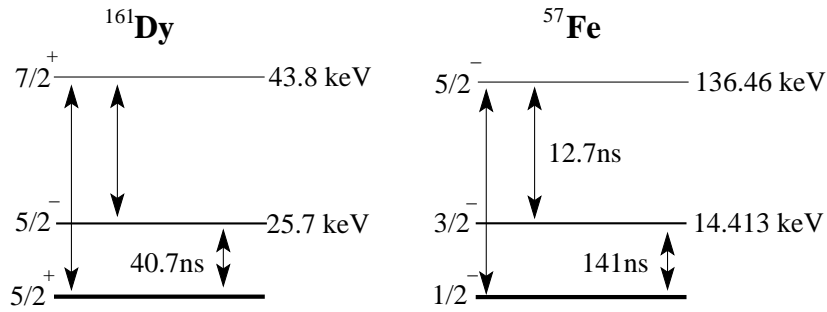
Figure 7 The Fe and Dy nuclear scheme.

Mössbauer Spectroscopy

Mössbauer spectroscopy refers to the resonant and recoil-free emission and absorption of γ-ray photons by atoms bound in a solid form [38]. It can be applied to the measurement of frequency with very high accuracy. The basic idea of the *Mössbauer Effect* is demonstrated in figure 8. In conventional Mössbauer spectroscopy a source nucleus in an excited state makes a transition to its ground state by emitting a γ-ray. The γ-ray is subsequently caught by an unexcited absorber nucleus of the same species, which ends up in the same excited state. The absorber emits a resonant photon with energy, E_γ after nuclear decay. The relative velocity, v, between the radioactive source and sample absorber is varied introducing a Doppler shift between the corresponding resonance energies. A detector behind the sample measures the

transmission as a function of the Doppler shift. The resulting spectrum gives information about the nuclear level splitting in the sample and the line width, Γ [37].
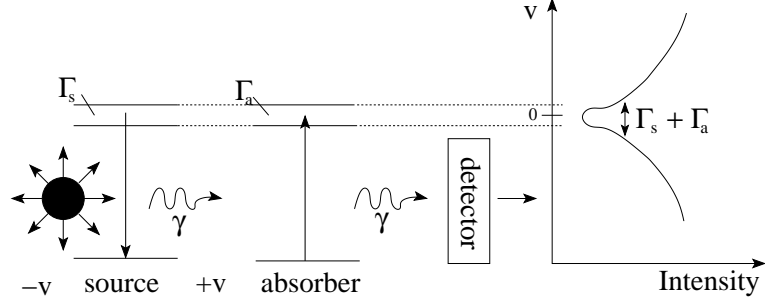
Figure 8 Principle of conventional Mössbauer spectroscopy.

Recoil during the emission and/or absorption process makes resonant fluorescence impossible. However, if the nucleus is bound in a crystalline structure, the solid as a whole can take up the recoil momentum leading to negligible recoil energy.

Energy and momentum conservation results in an upward shift of the nuclear transition energy called the recoil energy, E_R: The magnitude of the nuclear recoil momentum, p_n, after the emission must equal the magnitude of the momentum, p_γ, carried by the emitted γ-ray [37].

$$p_\gamma = \frac{E}{c} = p_n = \sqrt{3ME_R} \qquad (3.1)$$

$$E_R = \frac{E^2}{2Mc^2} \qquad (3.2)$$

With the advances and particular properties of synchrotron radiation Mössbauer experiments can be preformed using a time-resolved technique instead of the conventional energy-resolved technique. This technique is called synchrotron Mössbauer

spectroscopy (SMS) or nuclear forward scattering (NFS). Figure 9 describes monochromatic x-rays, E, interacting with a fixed ^{57}Fe nucleus. Part (a) describes the nuclear transition from the ground state, g, to the excited state, e, causing a sharp resonance in the excitation probability density, S(E) shown on the right. The emitting nucleus can also interact with the atoms of a solid and participate in lattice vibrations. This is shown in part (b) of figure 9. Not only is there a zero phonon Mössbauer peak, but there are side bands due to the phonon contribution. This phenomena is the basis of NRIXS described in the upcoming sections.

(a) Fixed Nucleus:
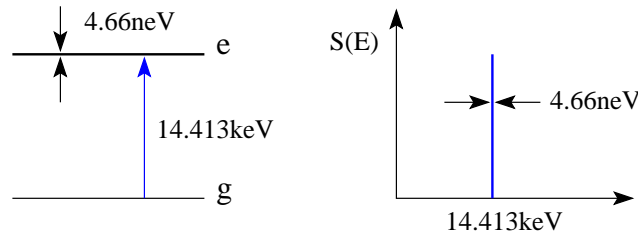
(b) Nucleus & simple
    lattice excitation:
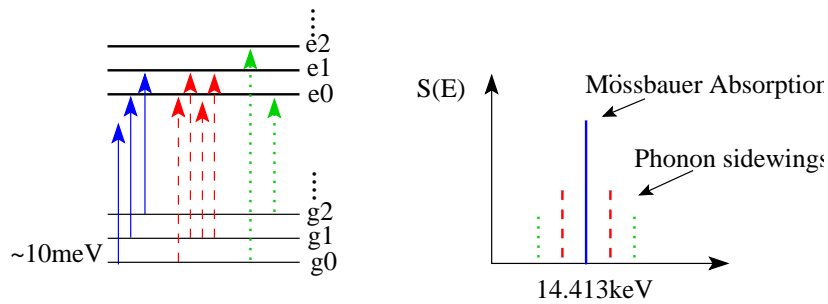
Figure 9 Excitation of the ^{57}Fe resonance as adapted from W. Struhahn [39].

Scattering Processes

There are many underlying scattering processes that take place in nuclear resonant experiments. Figure 10 below summarizes the classification scheme, which is based on the analysis of the initial and final states of the scatterer [40].
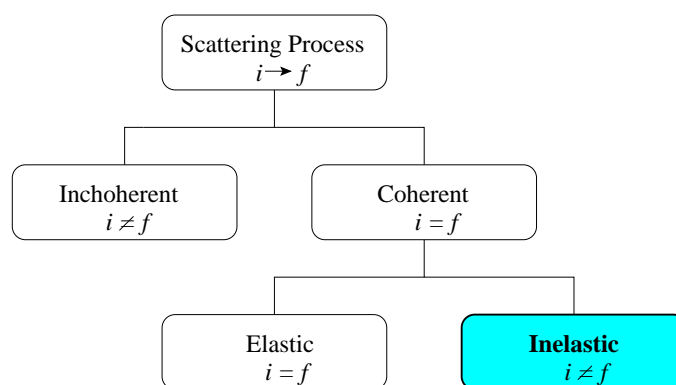
Figure 10 Flow chart of scattering process where, i, is the initial state and f, is final state.

Incoherent scattering $(i \neq f)$ is due to a change in core states (the state of the nucleus and inner electron shell of the atom). This process is of no interest to the experiments described in this thesis.

Coherently scattering $(i = f)$ occurs when all core states are left unchanged. Essentially, the photon cannot determine which atom it scattered from. The coherent process is divided into two sub-scattering processes, elastic and inelastic. These processes provide information about the collective state of the lattice vibrations.

Elastic scattering $(i = f)$ occurs when the photon has the same initial and final energy. It is coherent elastic scattering that causes resonant excitations of the nucleus as described in figure 9, the Mössbauer effect.

17

The inelastic scattering ($i \neq f$) process defines an energy transfer between the photon and the atom causing the photon to have a different initial and final energy.

Nuclear Inelastic Scattering

The nucleus is vibrated by an x-ray pulse of specific incident energy. After the pulse the solid continues to vibrate creating phonons. Resonant excitation can only take place when the incident energy plus the energy exchanged with a particular vibrational mode equals the resonance energy, E_γ. If the incident energy is less than the resonant energy then phonon energies are added to achieve the resonant energy (figure 11, part a). If the incident energy is more than the resonant energy then phonon energies are subtracted to equal the resonant energy (figure 11, part b).

The presence of phonons leads to increased transition energies when phonon creation occurs ($E_0 + n$), and to decreased transition energies ($E_0 - n$) when phonon annihilation occurs. Figure 11, part c, shows a sharp peak with width, Γ, around the nuclear transition energy, E_0. This peak is a direct result of the recoil-less absorption of x-rays by the nucleus; the well-known Mössbauer effect. In addition to the peak at the nuclear transition energy, S(E) also features side wings. The side wings describe the excitation probability per unit energy interval due to phonons, S(E) [40]. This results in three main energy scales involved (table 1):

transition energy (keV) $\longleftrightarrow$ phonon energy (meV) $\longleftrightarrow$ nuclear level width (neV)

Isotope	^{57}Fe	^{161}Dy
Nuclear Resonance (E_γ)	14.143 keV	25.651 keV
Recoil Energy (E_R)	1.9 meV	2.2 meV
Nuclear Level Width (Γ)	4.67 neV	16.2 neV
Half-Lifetime ($\tau_{1/2}$)	97.8 ns	28.2 ns
Natural Isotope Abundance	2%	18.8%
Resonant Cross Section (σ_0)	256 10^{-20}cm^2	95 10^{-20}cm^2

Table 1 Properties of ^{161}Dy and ^{57}Fe [5].
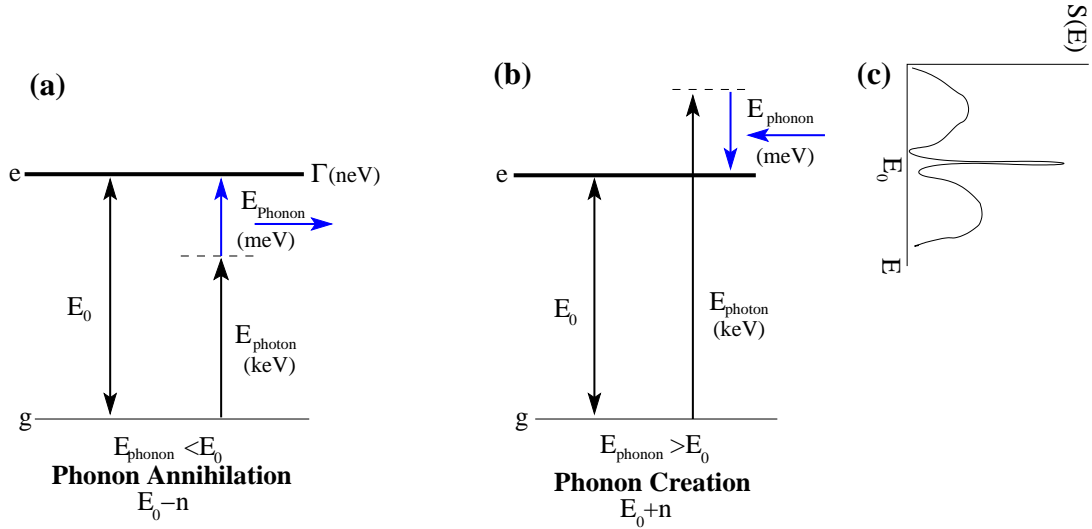
Figure 11 Resonant excitation takes place with the assistance of phonon annihilation or phonon creation. (a) Annihilation: taking a phonon to boost the incoming energy to the resonant energy. (b) Creation: Creating a phonon to subtract from the incoming energy to achieve the resonant energy. (c) How phonon creation/annihilation is translated to the excitation probability density, S(E) creating side wings. Note that the transition energy in the keV range is only being affected by a phonon in the meV range.

Determining S(E)

The experimental flux, I(E), detected is the atomic fluorescence following the internal electron conversion. It is given by equation 3.3, where ϵ specifically denotes

the energy of the incident x-rays relative to the nuclear transition energy ($\epsilon = E - E_0$) [39, 40, 41, 42, 43, 44, 45].

$$I(\epsilon) = I_0 d\rho \frac{\eta\alpha}{1+\alpha}\sigma\left(\epsilon\right) \tag{3.3}$$

Where,
I_0: incident photon flux
d : detection efficiency
ρ : effective area density of the nuclei
η : fluorescence yield
α: internal conversion coefficient
$\sigma(\epsilon)$ is the cross section from nuclear resonant excitation of a photon with energy, ϵ.

It is based on the probability of observing phonons. It indicates that the interacting cross-section of incident photons with the sample during the phonon exchange is related to the nuclear level width, Γ and the phonon excitation probability, S(E). It is described by:

$$\sigma(\epsilon) = \sigma_0 \Gamma \frac{\pi}{2} S\left(\epsilon\right) \tag{3.4}$$

Where,
σ_0: maximum resonant cross section, (equation 3.5)
Γ: Nuclear level width
$S(\epsilon)$: Excitation probability per unit energy interval due to phonons

$$\sigma_0 = \frac{\lambda^2}{2\pi} \frac{1 + 2I_e}{1 + 2I_g} \frac{1}{1+\alpha} \tag{3.5}$$

λ: x-ray energy
I_e, I_g: nuclear spins of the excited and ground states

Feasibility of Detection

The probability for recoil-less absorption, the Lamb-Mössbauer factor, is given by: $f_{LM} = \Gamma S(\epsilon = 0)$. The value of f_{LM} varies between 0.05 and 0.9 for solids at room temperature but vanishes for liquids and gases [40]. By lowering the temperature or increasing pressure, f_{LM} increases as a result of the average number of phonons decreasing [35].

The estimate for absorption 'on resonance' is therefore:

$$\sigma(0) = \frac{\pi}{2}\sigma_0 f_{LM} \tag{3.6}$$

With the exception of the elastic peak, S(E) is expected to be a smooth function in energy extending over an energy range that may be estimated by the Debye energy, Θ. This is demonstrated in figure 12. Using the normalization of S(E), the "off-resonance" region can be estimated by:

$$\Theta S(\epsilon) \approx 1 - f_{LM} \tag{3.7}$$

Plugging into equation 3.6 gives

$$\sigma(\epsilon \neq 0) = \frac{\pi}{2}\sigma_0(1 - f_{LM})\frac{\Gamma}{\Theta} \tag{3.8}$$

A quantitative estimate for ^{57}Fe in metallic form gives in units of the photoelectric cross section [39].

$\sigma(0) \approx 560\sigma_{pe}$, $\sigma(\epsilon \neq 0) \approx 0.0002\sigma_{pe}$

Near the elastic peak of experimental spectrum ($\epsilon = 0$), the penetration depth of the x-rays in the sample is dominated by the nuclear resonant absorption cross section. This situation leads to a suppression of the elastic peak in the measured data

by an unknown factor; it cannot be normalized by simply integrating the spectrum. Instead, the elastic peak is replaced by what is theoretically expected [44, 45]. This is described in Chapter 5: Data Evaluation Procedure.
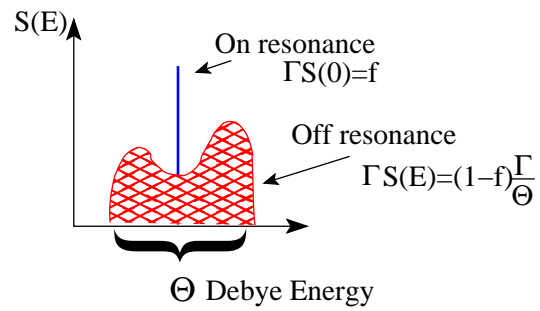
Figure 12 Feasibility of detection.

CHAPTER 4

SYNCHROTRON RADIATION

After the Mössbauer Effect was discovered in 1957, Sing and Visscher developed a theoretical basis for extracting lattice dynamics from Mössbauer measurements [42, 43]. Experimental attempts were made to measure the atomic vibration frequency distribution, the phonon density of states. Due to weak radiation sources, typical phonon energy transfers could not be reached with accuracy using the conventional Mössbauer method [35].

The rapid development of this new spectroscopy and its application to high pressure became possible with the unique properties of synchrotron radiation at third generation sources such as the Advanced Photon Source (APS) at Argonne National Laboratory in Chicago, IL [41, 40, 46, 47]. A brief introduction to the key features and uniqueness of synchrotron radiation in relation to nuclear resonant scattering is presented.

Key Features

Synchrotron radiation is produced by means of the following procedure. A Barium Aluminate $(Ba(AlO_2)_2)$ cathode is heated to produce electrons. This "electron gun" produces electrons in "bunches". A radio frequency cavity further defines the "bunches" by slowing down the fast electrons and "cutting off" the slow electrons for the next bunch. The actual pattern of bunches produces the time structure of the synchrotron radiation. This timing structure of electrons can be modified depending on the experiment. The standard time structure at the Advanced Photon Source consists of 23 bunches with a separation of 153 ns. It is very important for NRIXS experiments that the time between bunches is larger than the dead time of the detector (20 ns) and at least comparable to the nuclear lifetime, Γ of the isotope in order to obtain appreciable signal rates. A linear accelerator (LINAC) is used to accelerate

23

and compact the bunch again into a "bucket" with a radio frequency microwave field. At this point the electrons have energy in the MeV range. From the LINAC the electrons go into a booster synchrotron, which increase the energy to the GeV range before going into the storage ring. To keep the electrons in a closed orbit they have to be accelerated perpendicular to their propagation direction. At the Advanced Photon Source, electrons with energy of 7 GeV are kept on a approximately circular orbit of circumference 1.1 km using bending magnets. Bending magnets allow the electrons to be accelerated and emit electromagnetic radiation while going around the bend [48]. A general schematic of a synchrotron facility is shown in figure 13.

Insertion Devices

The x-rays produced by the bending magnets are moderately intense. Very high brilliance synchrotron radiation, sufficient for NRIXS experiments, is generated from undulators. An undulator is an insertion device that is straight and has shorter periods relative to the bending magnets. As the electrons propagate through the field they experience small periodic deviations from a straight line. The accelerations exerted by the periodic field create radiation that adds up coherently to produce an emission of very collimated and intense x-rays.

Synchrotron radiation has a broad energy distribution. Using the appropriate undulators and monchromators allow for a wide range of energy tunability. This is essential for NRIXS experiments, which require tunability in the meV range around the Mössbauer nuclear resonance, E_γ.

Monochromators

Undulators create a broad energy band of x-rays (called "white beam") that ranges from about 6 keV up to several 100 keV. A high heat load (HHL) monochromator filters the energy and reduces the power of the broad energy band. It is designed
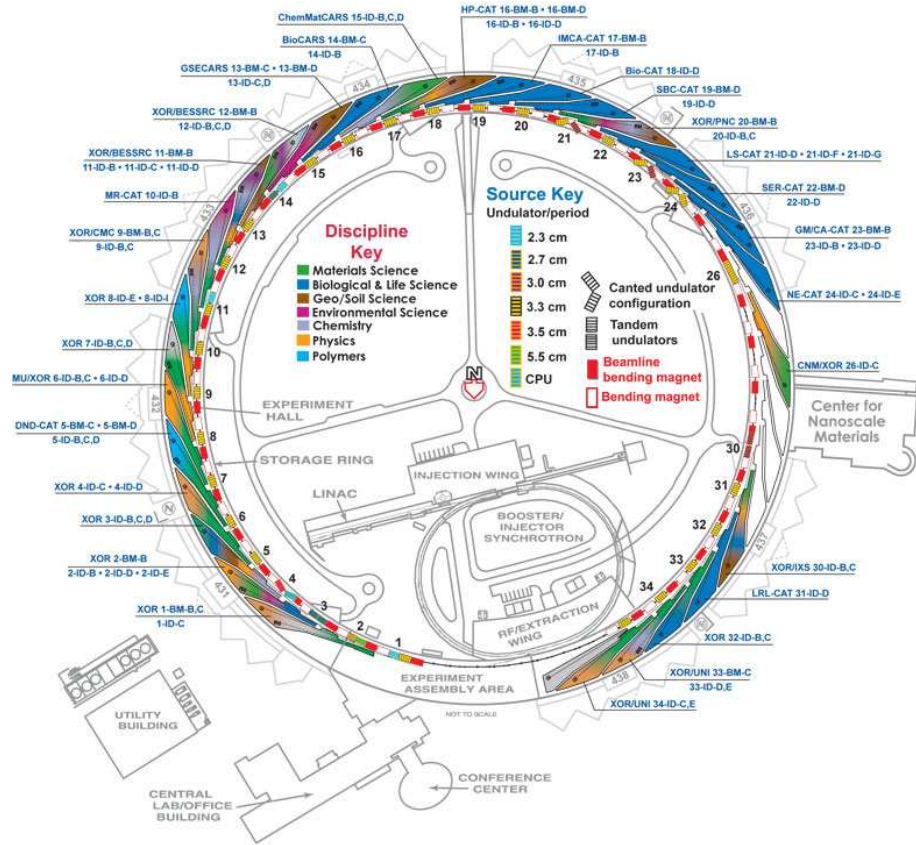
Figure 13 A schematic of the Advanced Photon Source synchrotron facility.

with perfect crystals that are positioned in a non-dispersive arrangement and operate at specific Bragg reflections. This is shown in figure 14. The HHL monochromator reduces the energy to a band of approximately 1 eV around the resonance energy of the specific isotope. This bandwidth is not narrow enough for performing phonon spectroscopy, but the total power of the x-ray beam is reduced from 1000 to 0.1 Watts [39]. To attain a narrower bandwidth, a high resolution (HR) monochromator is required. The high resolution monochromator is very temperature sensitive due to the thermal expansion of the crystals. Thus, the reduction in power from the HHL monochromator is necessary.

A high resolution monochromator is tunable around the resonant energy range (± 200 meV) where the probability for phonon excitation or annihilation is high.

To tune around the resonance the HR monochromator relies upon the use of Bragg diffraction from a series of perfect single crystals. The diffraction planes and their orientation with respect to the crystal surfaces are chosen to achieve optimal performance in terms of efficiency and energy. The energy resolution function of the HR monochromator is measured using coherent elastic nuclear resonant scattering (NFS). Further details about the criteria for HR monochromator designs and crystal selection are presented in the works by T. Toellner [49].

Synchrotron Radiation source: Undulator E:~100 keV   High Heat Load Monochromator 1 keV   High Resolution Monochromator 1 meV   Focusing Mirror   Sample & Detectors

Four Bounce Nested Design
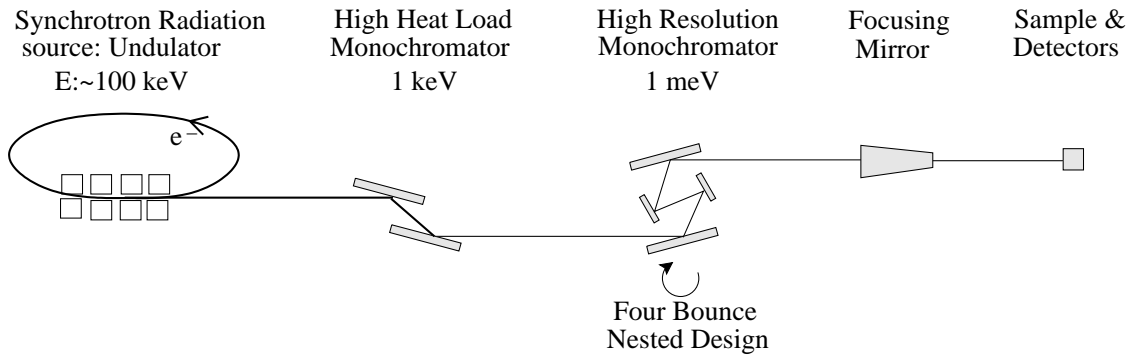
Figure 14 A general schematic of the experimental beamline setup. The synchrotron radiation comes from an undulator source with an energy range of 100 eV. The energy is reduced by the high heat load monochromator to an energy range of 1 eV around the resonant energy. The power is also reduced from 100 W to 0.1 W. The high resolution monochromator scans the energy ± 200 meV around the resonant energy. The focusing mirrors focus the beam to a small spot size.

Focusing

A mirror system is placed after the HR monochromator to focus the beam to a spot size on the order of the DAC sample chamber. A Kirkpatrick-Baez mirror configuration, as shown in figure 15, has been implemented at both beamlines. The mirror configuration consists of two independent grazing incidence mirrors with a slightly

elliptical shape. They are arranged with their surface normal nearly perpendicular to the incident x-ray and rotated 90° relative to each other. The first reduces to beam in the in the vertical direction and the second in the horizontal direction [50, 51].
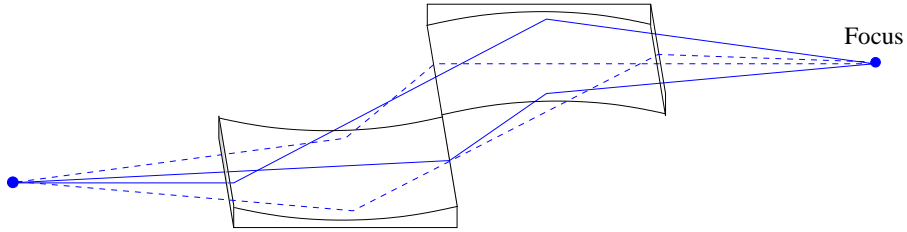
Figure 15 Kirkpatrick-Baez focusing mirror configuration.

Detection

One crucial component in the success of NRIXS experiments is the data collection. Due to the specific timing requirements of the experiments and the large scattering range the detectors should have a good efficiency. In the 16-bunch mode at the APS, a synchrotron pulse of 100 ps length strikes the sample every 176 ns. When this occurs there is a large amount of electronic scattering or non-resonant events. This is shown in figure 16. These events are of no interest; therefore the detector needs to start counting when all electronic scattering processes are completed. Within a few nanoseconds after the synchrotron pulse, the resonant phonon events start to occur. The avalanche photo-diode (APD) detector has a typical time resolution of about 1 ns making it a perfect candidate for NRIXS experiments [52]. Electronic noise created by the detector can occur which would look like false "delayed events." This background is unavoidable but typically small. The noise-event rate is independent of the incident x-ray energy and is measured by tuning the monochromator sufficiently

far away from the resonance. The nuclear resonant events scatter in a 4π area. The APD's are designed to have 10×10 mm^2 area which can detect most of the scattered events. The detectors are made of silicon and as a result have a high efficiently with low fluorescence energy therefore Dy and Fe with a fluorescence of ~6.5keV is detected with an efficiency of about 85% [53].
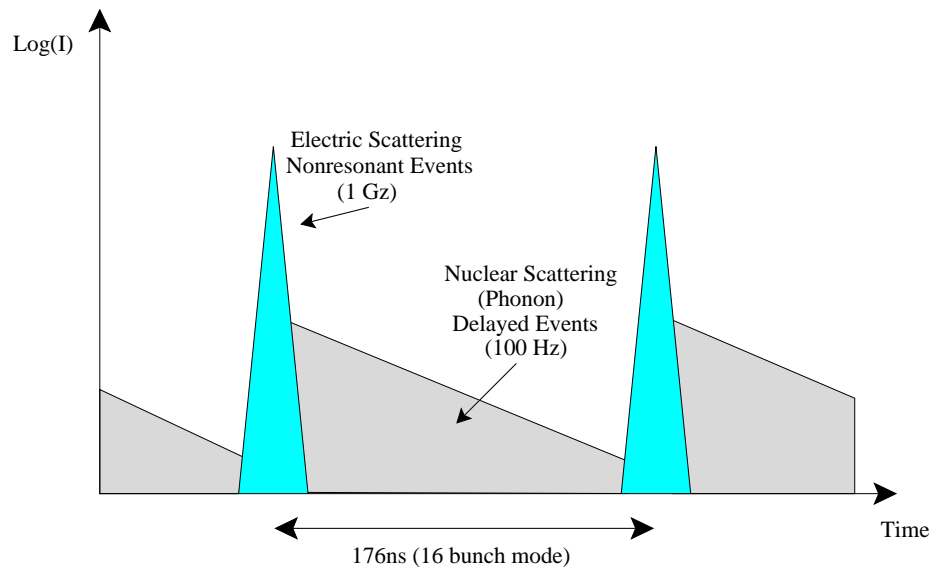
Figure 16 Simplified time spectrum. As an electron bunch hits the sample it creates a large peak shown as the non-resonant events. The detector is turned "off" during this time. Between bunches, the delayed events or resonant excitations occur in which the detector is then turned "on".

Beamline Specifics

The nuclear resonant inelastic x-ray scattering (NRIXS) experiments for both (^{57}Fe & ^{161}Dy) isotopes were preformed at the Advanced Photon Source (APS) at Argonne National Laboratory. Experiments for the ^{57}Fe isotope were collected using the High-Pressure Collaborative Access Team's (HPCAT) undulator beamline 16-ID-

D. It is single undulator of length 2.5 m and period of 3.3 cm. The [161]Dy isotope experiments were performed on the X-Ray Operations and Research group's (XOR) 3-ID-B undulator beamline. In contrast to 16-ID-D, a pair of undulators, each having a period of 2.7 cm was used. The combined undulator length of 4.4 meters increases the photon flux. To reach the [161]Dy resonance energy of 25.651 keV, the undulators third harmonic was used.

At both 16-ID-D and 3-ID-B, a high heat load monochromator, comprised of a pair of diamonds crystals was used. A four bounce nested design high-resolution monochromator was also used for both beamlines (configuration shown in figure 14). The design is comprised of two inner crystals of specific reflection nested in two more outer crystals of a specific reflection. At 16-ID-D silicon crystals with the (4 4 0) and (9 7 5) reflection were used. The resolution is about 1 meV at the full-width half-max (FWHM) at the [57]Fe resonant peak. The monochromator was used to scan around 14.4 keV energy range in steps of 0.5 meV. At 3-ID-B, the high-resolution monochromator engaged two pairs of silicon crystals cut in the (4 4 4) and (18 12 6) reflection plane [54]. These crystals achieved a higher resolution of 0.6 meV at the Dy resonance of 25.6 keV and scanned around the energy range ($\pm$80 meV) in a smaller step size of 0.2 meV. At both beamlines a Kirkpatrick-Baez mirror system was used to focus the beam. The x-ray beam was focused to a $21 \times 20 \mu m^2$ area for Dy and a $30 \times 50 \mu m^2$ area for Fe site experiments. Comparison of the beamline components are listed in table 2.

Beamline	16-ID-D	3-ID-B
Isotope	^{57}**Fe**	^{161}**Dy**
Energy Range	6-15 keV	7-27 keV
High Heat Load Monochromator	Di (111)	Di (111)
High Resolution Monochromator	Si (4 4 0) (9 7 5)	Si (4 4 4) (18 12 6)
Resolution	1 meV	0.6 meV
Focus	25 x 55 μm	10 x 20 μm

Table 2 Component properties of the beamlines used at the APS.

CHAPTER 5

EXPERIMENTAL DETAILS

Sample Preparation

The DyFe$_3$ sample was kindly prepared by Dr. Hubertus Giefers using UNLV facilities. The starting materials for preparing the dysprosium-iron inter-metallic compound were 98% enriched 57-iron and 98% enriched 161-dysprosium. The enriched ^{57}Fe was ordered from Advanced Material Technologies. The enriched ^{161}Dy sample was ordered from Oakridge National Laboratory. A combination of 25 at.% hand ground ^{161}Dy powder with 75 at.% ^{57}Fe powder were pressed into pellets, and melted several times in an arc-melting furnace under argon in a water-cooled copper crucible. The products were ground afterwards in an argon atmosphere to prevent oxidation and ignition [13].

The crystal structure and phase purity was studied by conventional x-ray powder diffraction. In the standard x-ray diffraction pattern, taken at UNLV, a contamination of DyFe$_2$ could be identified. However, the 3.8 volume % of DyFe$_2$ is significantly small. Pressure dependence of the structure was determined at the APS using angle dispersive x-ray diffraction (ADX) techniques with a non enriched sample. The ADX patterns of DyFe$_3$ indicated no phase transition up to 20 GPa. The a-axis is slightly more compressible than the c-axis and the c/a-ratio decreases by 0.9% from 4.797 to 4.841 between ambient conditions and 20 GPa [13].

High Pressure Technique for NIS

At ambient conditions the NRIXS spectrum was recorded with the sample prepared between two pieces of adhesive tape, which were than placed between two avalanche photo-diode detectors as shown in figure 17.

To achieve high pressure a diamond anvil cell (DAC) is used. The inelastically

scattered radiation is emitted in a 4π solid angle; therefore, the design of the diamond anvil cell has to be taken into consideration. These experiments were executed with a Paderborn-panoramic style diamond anvil cell (figure 18 and 19) [55]. This design has two large openings in the cylinder to allow the detectors to fit inside without compromising the ability to create pressure. The force is applied by turning 8 screws, allowing the applied pressure to be uniformly distributed.

In most NRIXS experiments the incident synchrotron beam is projected through the diamonds of the DAC onto the sample. The inelastic resonant excitations were observed by collecting the delayed quanta with two avalanche photo-diode detectors placed perpendicular to the beam (figure 20) [55, 56].
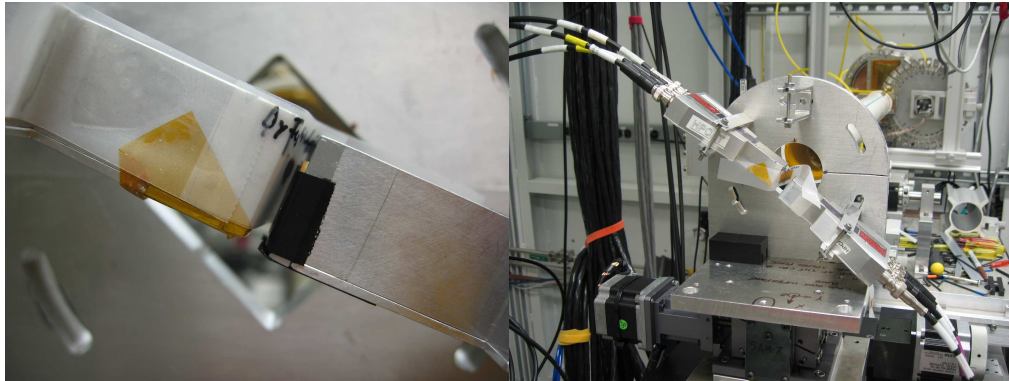
Figure 17 At ambient conditions the sample is placed between two pieces of tape. The detectors are placed very close to the tape.

SECTION A-A
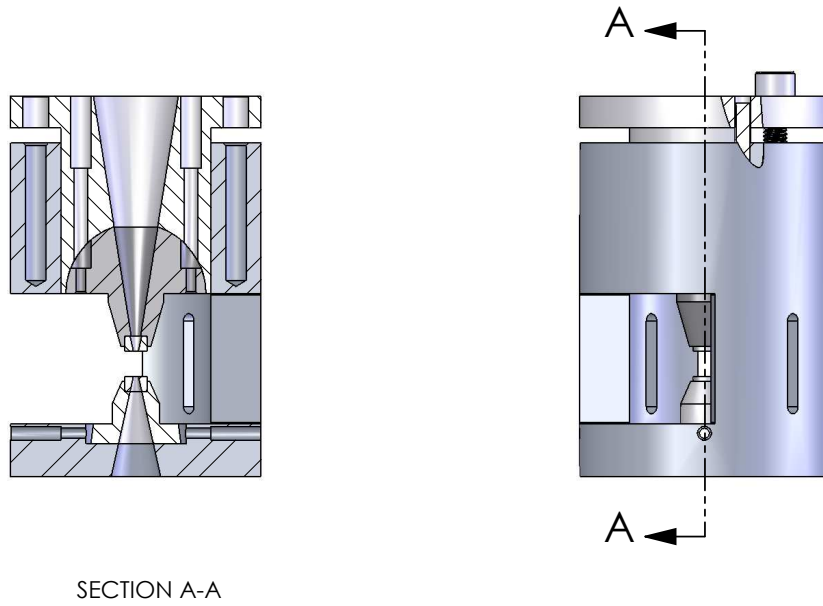
Figure 18 Schematic of the Paderborn-panoramic style diamond anvil cell.

Figure 19 Paderborn-panoramic style diamond anvil cell.
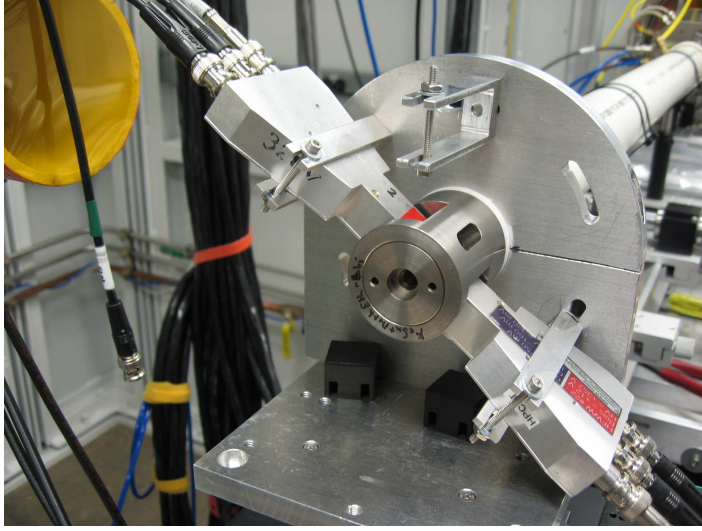
Figure 20 High pressure experimental setup. The sample is loaded into a DAC. The DAC is mounted in a holder and the detectors side into the large openings.

At all pressures the DyFe$_3$ sample, of $\sim$90 μm, was loaded in a beryllium gasket because the material is transparent to x-rays and will absorb very little signal [57]. A 4:1 methanol-ethanol mixture was used as a pressure transmitting medium and some spherical ruby crystals were used for pressure determination. One DAC was loaded for each desired pressure point. The objective was to use the same DAC at each beamline to ensure that the pressure and sample conditions were the same. However, due to long periods of time between experiments there were pressure fluctuations and exact conditions could not be achieved.

It is common at the APS, as well as UNLV, to use the ruby fluorescence R$_1$ line. It shifts with pressure almost linearly, according to equation 5.1 [58, 59]. Where B=7.665 for quasi-hydrostatic conditions. The R$_1$ wavelength is determined by fluorescing the ruby with a 401 nm laser. The R$_1$ wavelength and calculated pressures are listed in table 3.

$$P(GPa) = \frac{1904}{B}[(1 + \frac{\Delta\lambda}{\lambda_0})^B - 1] \qquad (5.1)$$

^{57}Fe		^{161}Dy	
Pressure (GPa)	Wavelength (nm)	Pressure (GPa)	Wavelength (nm)
0	694.33	0	694.33
3.5	695.60	3.7	695.73
9.5	697.74	8.7	697.45
19	701.05	19	701.05
30.4	704.87	35	706.40

Table 3 Ruby R_1 wavelengths and corresponding calculated pressures.

NIS Spectra

At ambient conditions (without use of the high pressure cell) the maximum counting rate for the Dy delayed signal was $\sim$1100 and $\sim$500 counts per second for Fe, when on resonance. As pressure increased the count rates decreased. At around 30 GPa the count rates for the Dy and Fe experiments were about the same; 20 counts per second on resonance. This resulted in the phonon counts to be around 7 counts per scan. To reach reasonable statistics, 20-30 scans, each collected in 60 minutes, were summed up for each pressure point.

The normalized NRIXS spectra of $DyFe_3$ at ambient conditions and under high pressure at 300 K is plotted in the figure 21. The ^{161}Dy contribution is on the left in red while the ^{57}Fe contribution is on the right in blue. The y-scale gives the normalized scattering probability (1/eV) by using Lipkin's sum rules [60]. In this figure there is a peak at the nuclear transition energy ($E - E_0 = 0$), and side wings due to the creation or annihilation of phonons. The difference in energy resolution between the HRM at 3-ID-B (0.5 meV) and 16-ID-D (1 meV) results in a narrower elastic peak width in the Dy measurements.

In evaluating the results, it is proper to consider the slight contribution (about 3%) of $DyFe_2$ to the $DyFe_3$ spectra. By collecting NRIXS data of $DyFe_2$ at the same pressure it could be subtracted from the $DyFe_3$ spectra. However as the contamination is less than 5% it can be included within the error and it's contribution is not subtracted from this data.
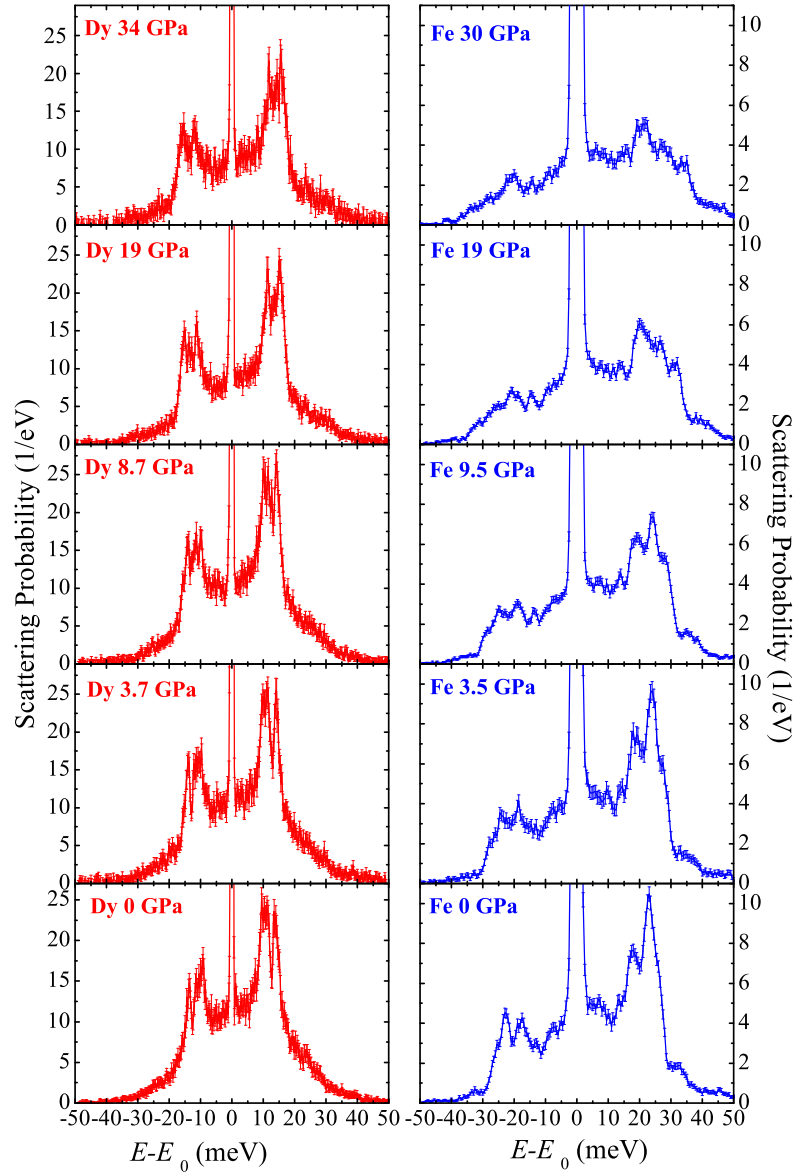
Figure 21 The normalized NRIXS spectra of DyFe$_3$ at ambient conditions and under high pressure at 300 K. The ^{161}Dy contribution is in red while the ^{57}Fe contribution is in blue. The y-scale gives the normalization of the data by using Lipkin's sum rules [60]. In this figure there is a peak at the nuclear transition energy ($E - E_0 = 0$), and side wings due to the creation or annihilation of phonons.

Data Evaluation Procedure

The experimentally measured flux, I(E), is proportional to the absorption probability, S(E), per unit of energy and to the effective number, η_{eff}, of the specific Mössbauer nuclei in the sample. Where the energy, E is given relative to E_0 [40].

$$I\left(E\right) = \text{cosnt} \cdot \eta_{eff} S\left(E\right) \text{ with } \int_{-\infty}^{\infty} S(E) dE = 1 \tag{5.2}$$

S(E) can be expanded in terms of n-phonon contributions where the elastic part is $S_{el}(E)$ and the inelastic part is $S_{in}(E)$ [40, 42].

$$S\left(E\right) = \underbrace{f_{LM}\delta E}_{S_{el(E)}} + \underbrace{f_{LM}\sum_{n=1}^{\infty} S_n\left(E\right) S\left(E\right)}_{S_{in}(E)} \tag{5.3}$$

The relative weight of the inelastic part is 1-f_{LM}. The phonon DOS, $g(E)$ is proportional to the single-phonon (n=1) term in the expansion of $S_{in}(E)$. The $n > 2$ terms are the multi-phonon contributions. They are obtained by the convolution of $S_{n>1}(E)$ with $S_1(E)$, according to the relations [61]:

$$S_1\left(E\right) = \frac{E_R g\left(|E|\right)}{E\left(1 - e^{-E/k_B T}\right)} \tag{5.4}$$

$$^* S_n\left(E\right) = \frac{1}{n}\int_{-\infty}^{\infty} S_{n-1}\left(E - \epsilon\right) S_1\left(\epsilon\right) d\epsilon, n \geq 2 \tag{5.5}$$

* convolution equation

There are four general steps in extracting the phonon DOS, $g(E)$, from I(E). They are demonstrated in figure 23. These steps are executed using the program PHOENIX written by W. Struhahn [62].

1. Normalization:

To normalize the spectra, the first moment of the Lipkin's sum rules is employed. It uses the general property of S(E), that the first moment is equal to the recoil energy, E_R, of a free nucleus [60, 63]. The elastic part, $S_{el}(E)$, is assumed to be symmetric around $E=0$, therefore it has no effect on the first moment.

$$\int S(E)EdE = E_R \tag{5.6}$$

therefore $\int_{-\infty}^{\infty} I(E)EdE$

$= const \int_{-\infty}^{\infty} \eta_{eff} S(E)EdE$

$= const \left[\underbrace{\eta_{eff}^{el} \int S_{el}(E)EdE}_{0} + \underbrace{\eta_{eff}^{in} \int S_{in}(E)dE}_{E_R} \right]$

$= const \cdot \eta_{eff}^{en} E_R$

$$I_{norm}(E) = \frac{E_R I(E)}{\int_{-\infty}^{\infty} I(E)EdE} \tag{5.7}$$

2. Removal of the elastic peak:

The PHOENIX program removed the elastic peak by generating a shape function internally based on a set of parameters. The parameters interpolate the experimental data in the elastic peak region about ∓ 3 meV [62]. The resulting spectrum is equivalent to the n-phonon part, $S_{in}(E)$, of the absorption probability. The integration gives the recoil fraction directly $(1 - f_{LM})$. As a result, f_{LM} can be determined without any knowledge about the number of Mössbauer nuclei in the sample.

3. Extracting the n-phonon contributions:

The inelastic spectrum is composed of the different n-phonon contributions, $S_n(E)$, for $n=1, 2, >3$. PHOENIX uses the convolution equation (5.5) to decompose these

contributions. The procedure begins with a first approximation of $S_n(E)$, and then with every additional step, there is a subtraction of a multi-phonon term. This procedure is repeated until the multi-phonon contributions get negligibly small [40]. The procedure is outlined in figure 22.
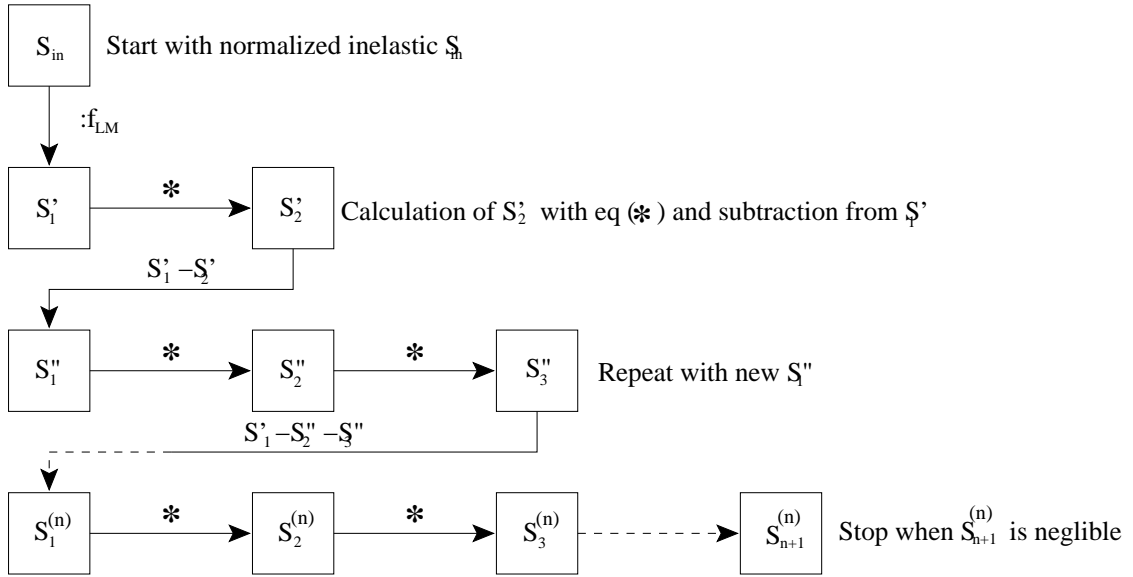
Figure 22 Recursion procedure for extracting the multi-phonon contributions.

4. Calculation of the phonon DOS

Finally, the phonon DOS, $g(E)$, can be calculated from the obtained $S_1(E)$ using equation 5.4.
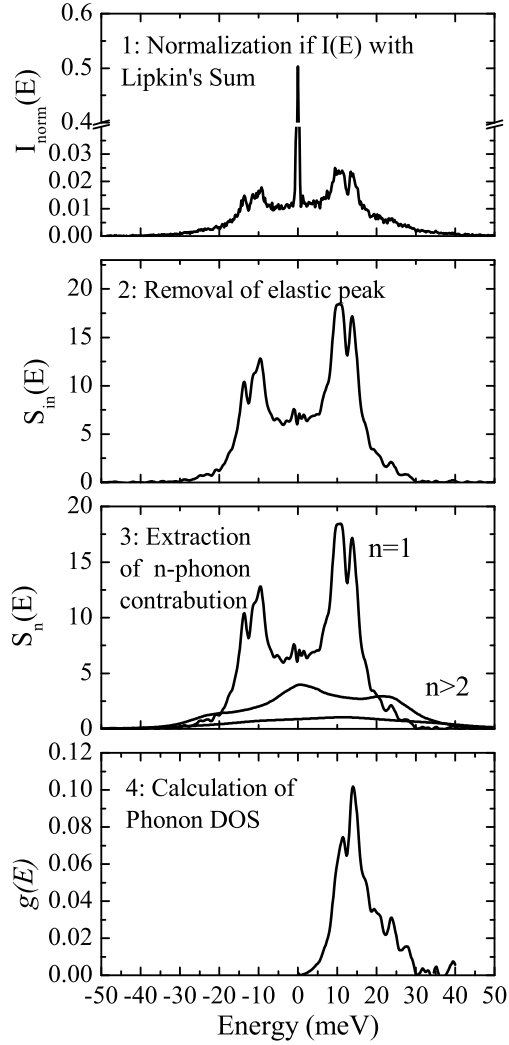
Figure 23 Steps to extracting of the phonon density of states as adapted from R. Lubbers [64]. In all parts the x-scale represents the energy difference relative to the resonance energy, $(E - E_0)$.

1. The inelastic spectrum is normalized using the Lipkin's sum rule [60, 63].

2. After removal of the elastic peak, the remaining inelastic part, $S_n(E)$, is the sum of single and multi-phonon contributions.

3. The multi-phonon contributions, $S_{n>2}(E)$, can be separated by a recursive procedure, equation 5.5.

4. The phonon DOS, $g(E)$, convoluted with the Gaussian resolution function, can be extracted from $S_1(E)$.

CHAPTER 6

RESULTS AND DISCUSSION

Extracted Phonon Density of States

The sample is polycrystalline, therefore the density of states (DOS) is a combination of all vibrational modes. In many cases, theoretical calculations are used to determine the dispersion relations of the vibrations that correlate to the experimental DOS. This was previously shown in figure 6. The normalized dual partial phonon DOS, $g(E)$, of ^{161}Dy and ^{57}Fe from the compound DyFe$_3$ are plotted together in figure 24. The red squares represent the ^{161}Dy partial phonon DOS on the lower energy side of the spectra while the blue circles represent the ^{57}Fe partial phonon DOS on the higher energy side of the energy spectra. The lattice stiffness is directly seen in the phonon density of states: the 11 meV low energy Dy mode does not shift; however the 16 meV Fe mode shifts to higher phonon energies as pressure increases.
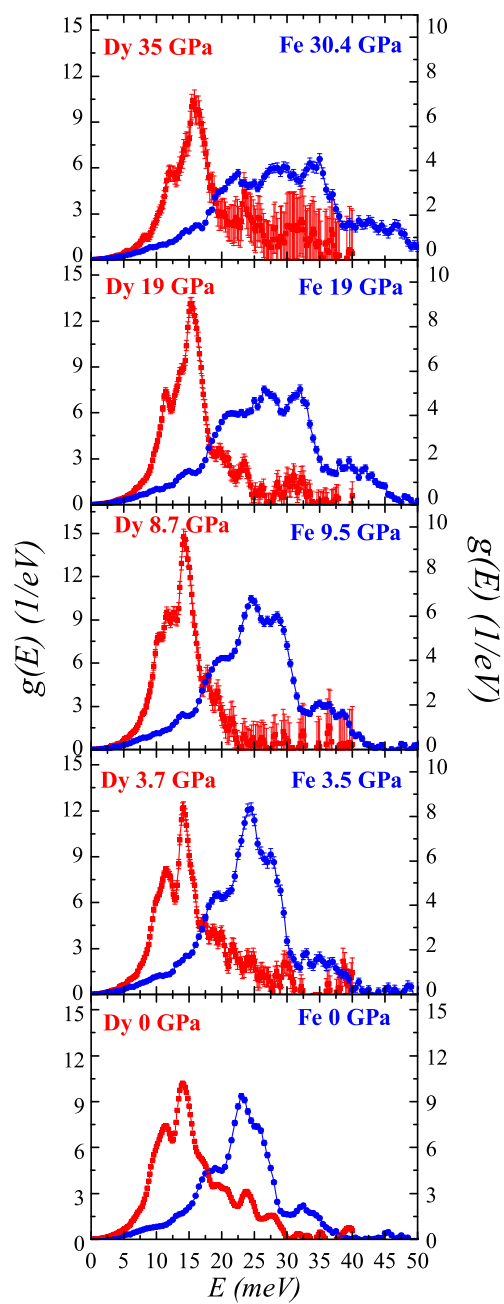
Figure 24 The normalized dual partial phonon DOS, $g(E)$, of DyFe$_3$. The red squares represent the ^{161}Dy partial phonon DOS and the blue circles represent the ^{57}Fe partial phonon DOS.

43

The [161]Dy partial phonon DOS for all pressures is plotted together and shown in figure 25. There are two strong peaks one around 11.45 meV and the other at 14 meV attributed to the two different Dy-sites (3a, 6c). The shape and peak positions stay comparitively the same as pressure increases except at 19 GPa and 35 GPa where the higher energy peak shifts to 15.4 meV.

In contrast, the [57]Fe partial phonon DOS, shown in figure 25, shows a large shift to higher energies. The three different Fe-sites (3b, 6c, and 18h) contribute to the phonon peaks. The 18h site should dominate in the overall peak intensity due to the large number of Fe atoms compared to the other sites. At ambient conditions, the strong phonon mode with the center of gravity at about 24 meV shows a sub-structure with one peak at 21 meV and another lower peak around 25 meV. With increasing pressure the main peak becomes weaker and merges with the low energy contributions which start at about 18 meV.

Figure 25 The partial DOS of [161]Dy and [57]Fe of DyFe$_3$ plotted separately for each pressure.

Lattice Dynamics of DyFe$_3$ Under Pressure

Derived Properties

The phonon DOS, $g(E)$, is of fundamental importance for the study of lattice dynamics. Its knowledge provides information on the lattice rigidity as well as thermodynamic properties. Each dynamical or thermal property of the solid depends on a different way in which the phonon frequency spectrum is weighted. For instance, the mean 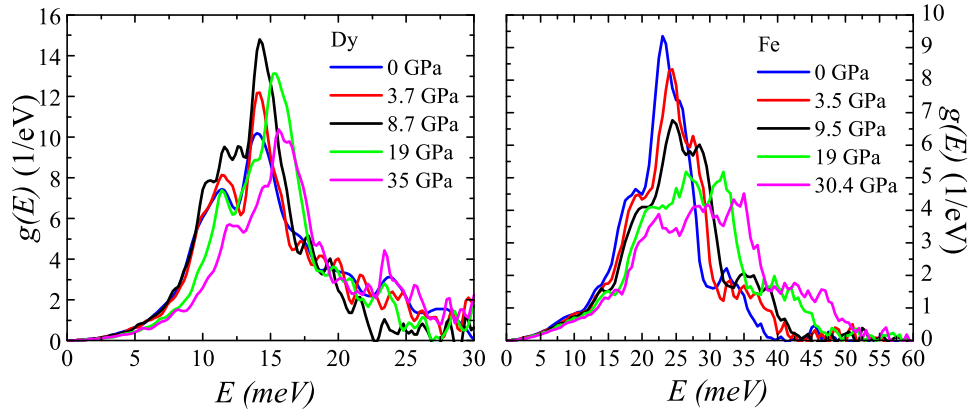square displacement and the recoil-less fraction are mainly determined by the low frequency phonons. Whereas the internal energy and high temperature Debye temperature is more sensitive to the high-frequency phonons.

The various lattice and thermodynamic properties that were calculated are summarized in table 4 at the end of the section [5]. The pressure point from the Dy site at 8.7 GPa is bracketed due to the fact that the calculated properties do not seem to correspond to the rest of the data. Further investigation in needed to determine the cause of this anomaly.

Most of these thermodynamic or elastic properties can also be theoretically calculated or simulated by a variety of modern computational methods like density functional theory [5].

Lattice Rigidity

An important parameter extracted from the phonon density of states is the Lamb-Mössbauer recoil-less emission factor, f_{LM}. As pressure increases the lattice becomes rigid and the recoil decreases. This is shown in figure 26 where the recoil-less factor increases. This factor comes directly from normalizing the inelastic spectrum and equating the recoil energy to the first moment of the inelastic spectrum [40, 60]. It is calculated by the following formula:

$$f_{LM} = e^{[-E_R \int_0^\infty \frac{g(E)}{E coth(x)} dE]}$$

(6.1)

The Lamb-Mössbauer factor is used to calculate the mean-square displacement of the atoms. While the nucleus is in its excited state, an atom will have vibrated at least several hundred times around its equilibrium position. Although, $< u >$ and $< v > = 0$ the mean square displacement, $< u^2 >$ and mean square velocity, $< v^2 >$ are non zero. The amplitude of the atomic vibration is of the order of 0.1 Angstrom which is typical for most solids at room temperature. The mean-square displacement is calculated from the following formula:

$$< \Delta x^2 >= -\frac{ln(f_{LM})}{k^2} \tag{6.2}$$

k = 7.31 Å^{-1} of the 14.413 keV quanta

k = 12.99 Å^{-1} of the 26.45 keV quanta

As shown in the figure 26, the larger the recoil-less factor is, the smaller the mean-square displacement, and the stiffer the lattice. The pressure effects on the lattice dynamics from 0 GPa to 30 GPa (35 for Dy) are more pronounced in the mean-square displacement, than the recoil-less factor, which is reduced by 30% in Fe and 25% in Dy.

The mean force constant, D, defined by the third moment of the Lipkin's sum, also reflects the hardening of the crystal lattice:

$$D = \frac{M}{\hbar^2} \int_0^\infty g(E)E^2 dE \tag{6.3}$$

In the investigated pressure range, D shows a strong increase from 122 N/m to 207 N/m for Fe and from 177 N/m to 241 N/m for Dy.

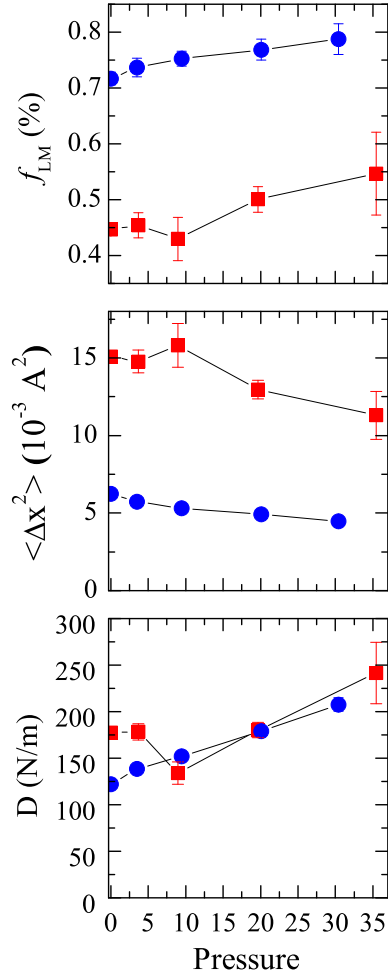Figure 26 The Lamb-Mössbauer factor, f_{LM}, mean-square displacement, $<u^2>$, and mean force constant, D calculated from $g(E)$. The blue dots represent Fe and the red squares represent Dy. The lines are to guide the eye

Thermodynamic Properties

The Helmholtz free energy, F_{vib}, is a thermodynamic potential which measures the "useful" work obtainable from a closed thermodynamic system at a constant temperature and volume. The pressure-induced increase of F_{vib} and the internal energy, U_{vib}, is shown in figure 27. They are calculated using the experimental DOS by equations 6.4 and 6.5 [5].

$$F_{vib} = 3k_B T \int_0^\infty g(E)ln[2sinh(x)]dE \tag{6.4}$$

$$U_{vib} = F - T\left(\frac{\partial F}{\partial T}\right)_v = \frac{3}{2}\int_0^\infty g(E)Ecoth(x)dE \tag{6.5}$$

The heat capacity, c_v, of a solid at constant volume is conventionally defined $c_v = \left(\frac{\partial U}{\partial T}\right)_v$ where U is the average internal energy of the solid. It has two contributions, one from lattice vibrations and the other from the thermal motion of electrons. Using the experimental DOS the vibrational contribution is calculated by equation 6.6:

$$c_v = 3k_B \int_0^\infty g(E)x^2 sinh^{-2}(x)dE \tag{6.6}$$

Where,

$x = E/(2k_B T)$

k_B is the Boltzmann constant

$E_R = 1.958$ meV the recoil energy of the ^{57}Fe nucleus (Dy, $E_R = 2.2$ meV)

$M = 9.4543 10^{-26}$ kg the mass of the ^{57}Fe nucleus (Dy, M $= 2.674 10^{-25}$ kg)

The vibrational entropy, S_{vib}, can be calculated from the experimental DOS by:

$$S_{vib} = -\left(\frac{\partial F}{\partial T}\right)_v = 3k_B \int_\infty^0 g(E)xcoth(x) - ln[2sinh(x)]dE \tag{6.7}$$

The decrease of c_v and S_{vib} can be interpreted in terms of a decreasing effective crystal temperature at high pressure. This effective crystal temperature can be defined as the ratio $T = \Theta_D$ of the real temperature, T, and the Debye temperature, Θ_D. The Debye temperature is discussed in the next section.
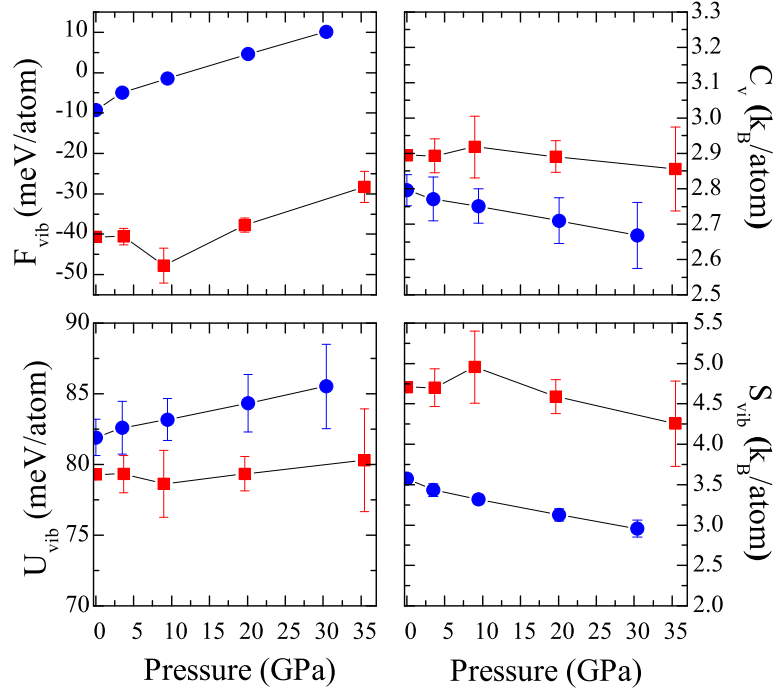
Figure 27 Thermodynamic properties of iron (blue circles) and dysprosium (red squares) at T=300 K derived from $g(E)$: lattice contribution to Helmholtz free energy, F_{vib}, internal energy, U_{vib}, specific heat, c_v and entropy, S_{vib}. The lines are to guide the eye.

49

Debye Temperature, Θ_D

The Debye temperature is a temperature independent parameter that corresponds to the cutoff frequency on the DOS curve. The high temperature Debye temperature describes the hardness of the investigated system.

$$\Theta_{D,HT} = \frac{4}{3k_B} \int_0^\infty g(E)E\,dE \tag{6.8}$$

The low temperature Debye temperature ($\Theta_{D,LT}$) is extracted from the partial phonon DOS at low energies, where the relation $g(E) = \alpha E^2$ is valid.

$$\Theta_{D,LT} = \frac{1}{k_B} \sqrt[3]{3\alpha} \tag{6.9}$$

They are both plotted in figure 28.
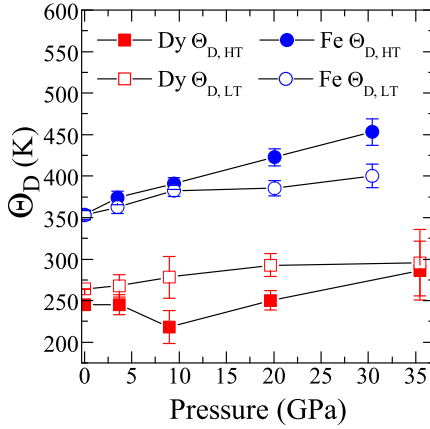
Figure 28 The high (closed symbols) and low (open symbols) temperature Debye temperature for Fe (blue) and Dy (red). The lines are to guide the eye.

Sample	p	f_{LM}	$<\Delta x^2>$	D	F_{vib}	U_{vib}	c_v	S_{vib}	$\Theta_{D,HT}$	$\Theta_{D,LT}$
DyFe$_3$	(GPa)	(%)	(10^{-3}A^2)	(N/m)	(meV/at.)	(meV/at.)	(k$_B$/at.)	(k$_B$/at.)	(K)	(K)
	0	0.716	6.23	122	-9.26	81.9	2.80	3.58	353	353
	3.5	0.773	5.72	138	-4.96	82.6	2.77	3.43	374	363
^{57}**Fe**	9.5	0.753	5.32	152	-1.42	83.2	2.75	3.32	391	382
	20.1	0.769	4.92	179	4.61	84.3	2.71	3.13	423	385
	30.4	0.787	4.48	208	10.14	85.5	2.67	2.96	453	400
	0	0.447	15.08	177	-40.68	79.3	2.894	4.70	245	264
	3.7	0.454	14.77	178	-40.56	79.3	2.893	4.70	245	268
^{161}**Dy**	(8.7)	0.430	15.81	134	-47.77	79.6	2.918	4.96	218	278
	19.6	0.501	12.95	180	-37.72	79.4	2.891	4.59	250	293
	35.5	0.547	11.3	242	-28.28	80.3	2.856	4.26	286	296

Table 4 Properties derived from the experimental DOS, $g(E)$ [5].

CHAPTER 7

CONCLUDING REMARKS

The method of nuclear resonant inelastic scattering of synchrotron radiation has been successfully applied to investigate the lattice dynamics of $DyFe_3$ under pressure. The dual partial phonon density of states was experimentally determined for two separate Mössbauer isotopes in the same compound for the first time at high pressure. The element selectivity and the ability to measure low concentrations of the sample makes the nuclear inelastic x-ray scattering technique and excellent tool to study local vibrational dynamics, not only in compounds but in impurities, dopants and interfaces.

From the partial density of states a variety of thermodynamic parameters, such as the Debye temperatures, the Helmholtz free energy and the vibrational contributions to the specific heat and the entropy were derived. This information cannot be as easily obtained with any other experimental technique. Understanding dynamics under high pressures is of great significance for geophysics and planetary astronomy.

Nuclear inelastic scattering yields an increase in the demands for precise *ab initio* calculations. The experimental data can be used as a tool for testing the accuracy of these calculations.

REFERENCES

[1] Shvyd'ko, Y.V., Gerken, M., Franz, H., Lucht, M., and Gerdau, E., Europhys. Lett. **56**, 309 (2001).

[2] Brown, D.E., Toellner, T.S., Sturhahn, W., Alp, E.E., Hu, M., *et al.*, Hyperfine Inter. **153**, 17 (2004).

[3] Chumakov, A.I., Rüffer, R., Leupold, O., Barla, A., Thiess, H., *et al.*, Phys. Rev. B **63**, 172301 (2001).

[4] Long, G.J., Hermann, R.P., Grandjean, F., Alp, E.E., Sturhahn, W., *et al.*, Phys. Rev. B. **71**, 140302 (2005).

[5] Alp, E.E., Sturhahn, W., Toellner, T.S., Zhao, J., Hu, M., and Brown, D.E., Hyperfine Interactions **144**, 3 (2002).

[6] Hu, M.Y., Sturhahn, W., Toellner, T.S., Mannheim, P.D., Brown, D.E., *et al.*, Phys. Rev. B. **67**, 094304 (2003).

[7] Van Der Goot, A.S. and Buschow, K.H.J, J. Less-Common Metals **21**, 151 (1970).

[8] Dariel, M.P. and Erez, G., J. Less-Common Metals **22**, 360 (1970).

[9] Oesterreicher, H. and McNeely, D., J. Less-Common Metals. **53**, 235 (1977).

[10] Bara, J.J., Pedziwiatr, A.T., and Zarek, W., Magnetism and Magnetic Materials **27**, 168 (1982).

[11] Yabe, H. and Kuji, T., J. of Alloys and Compounds **408**, 313 (2006).

[12] Liao, L.X., Altounian, Z., and Ryan, D.H., Phys. Rev. B **47**, 11230 (1993).

[13] Giefers, H., Unpublished Data (2006).

[14] Abeles, T.P., Bos, W.G., and Ouseph, P.J., J. Phys. Chem. Solids **30**, 2159 (1969).

[15] Van Der Kraan, A.M., Van Der Velden, J.N.J., Van Apeldoorn, F., *et al.*, Phys. Stat. Sol. **35**, 137 (1976).

[16] Psxczola, J., Zukrowski, J., and Krop, K., Magnetism and Magnetic Materials **44**, 223 (1984).

[17] Long-huan, J., James, W.J., Rhyne, J. and Lemaire, R., Chinese Phys. Lett. **2**, 253 (1985).

[18] Herbst, J.F. and Croat, J.J., J. Appl. Phys. **53**, 4304 (1982).

[19] Plusa, D., Pfranger, R., and Wyslocki, B., J. Magnetism and Magnetic Materials **40**, 271 (1984).

[20] Plusa, D., J. Magnetism and Magnetic Materials **51**, 331 (1985).

[21] Kunesh, C.J., Narasimhan, K.S.V.L., and Butera, R.A., J. Phys. Chem. Solids **34**, 817 (1973).

[22] Norgren, S., Hodaj, F., Azay, P., and Colinet, C., Metalurgical and Materials Trans. **29A**, 1368 (1988).

[23] Abbundi, R., Clark, A.E., Savage, H.T., and McMasters, O.D., Magnetism and Magnetic Materials **2**, 595 (1980).

[24] Bridgman, P.W., Proc. Am. Acad. Arts Sci. **81**, 167 (1952).

[25] Bridgman, P.W., and Simon, I., J Appl Phys **24**, 405 (1953).

[26] Van Valkenburg, A., *High-Pressure Microscopy*, in Giardini AA, Lloyd EC (eds), 87 (1963).

[27] Piermarini, G.J., *Static Compression of Energetic Materials*, Springer-Verlag Berlin Heildelberg (2008).

[28] Van Valkenburg, A., Appl. Opt. **9**, 1 (1970).

[29] Forman, R.A., Piermarini, G.J., Barnett, J.D., and Block, S., Science **176**, 284 (1972).

[30] Barnett, J.D., Block, S., and Piermarini, G.J., Rev. Sci. Instrum. **44**, 1 (1973).

[31] Klotz, S., Chervin, J-C., Munsch, P., and Le Marchand, G., J. Phys. D: Appl. Phys. **42**, 075413 (2009).

[32] Kittel, C., *Introduction to Solid State Physics*, John Wiley & Sons, Inc. **7**th **ed**. (1996).

[33] Ziman, J.M., *Principles of the Theory of Solids*, Cambridge University Press, **2**nd **ed**. (1972)

[34] Giefers, H., Tanis, E.A., Rudin, S.P., Greeff, C., Ke, X., Chen, C., *et al.*, Phys. Rev. Lett. **98**, 245502 (2007).

[35] Chen, Y.L., and Yang, D.P., *Mössbauer Effect in Lattice Dynamics*, WILEY-VCN Verlag GmbH & co. KGaA (2007).

[36] Liu, M., and Liu, L., High-Temperatures High-Pressures, **18**, 79 (1986).

[37] Eisberg, R., and Resnick, R. *Quantum Physics of Atoms, Molecules, Solids, Nuclei and Particles*, John Wiley & Sons, Inc. **2**nd **ed.**, (1985).

[38] Mössbauer, R.L.Z. Phys. **151**, 124 (1958).

[39] Sturhahn, W., J. Phys: Condens. Matter **16**, S497 (2004).

[40] Sturhahn, W., Toellner, T.S., Alp, E.E., Zhang, X., Ando, M., *et. al.*, Phys. Rev. Lett. **74**, 3832 (1995).

[41] Gerdau E. and de Waard H., *Nuclear Resonant Scattering of Synchrotron Radiation*, Hyperfine Interactions **123-125** (2000).

[42] Singwi, K.S., and Sjölander, A., Phys. Rev. **120**, 1093 (1960).

[43] Visscher, W.M. Ann. Phys. **9**, 194 (1960).

[44] Hu, M.Y., Toellner, T.S., Hession, P.M., Sutter, J.P., and Alp, E.E., Nucl. Instrum. Methods **428**, 551 (1999).

[45] Sturhahn, W., and Kohn, V.G., Hyperfine Interactions **123**, 367 (1999).

[46] Seto, M., Yoda, Y., Kikuta, S., Zhang, X.W., and Ando, M., Phys. Rev. Lett. **74**, 3828 (1995).

[47] Chumakov, A.I., Rüffer, R., Baron, A.Q.R., *et al.*, Phys. Rev. N. **54**, 9596 (1996).

[48] Mülhaupt, G., and Rüffer, R., Hyperfine Interactions **123**, 13 (1999).

[49] Toellner, T.S., Hyperfine Interactions **125**, 3 (2000).

[50] Kirkpatrick, P., and Baez, A.V., J. Opt. Soc. Am. **38**, 766 (1948).

[51] Eng, P.J., Newville, M., Rivers, M.L., and Sutton, S.R. *X-Ray Microfocusing: Applications and Techniques*, I. McNulty Eds., Proc. SPIE **3449**, 145 (1998).

[52] Barla, A., Rüffer, R., Chumakov, A.I., Metage, J., *et al.*, Phys. Rev. B. **61**, 22 (2000).

[53] Baron, A.Q.R., Nucl. Instrum. Methods **352**, 665 (1995).

[54] Toellner, T.S., Hu, M.Y., Bortel, G., Sturhahn, W., and She, D., Nucl. Instrum. Methods **A557**, 670 (2006).

[55] Giefers, H., Lübbers, R., Rupprecht, K., Wortmann, G., *et al.*, High Press. Res. **22**, 501 (2002).

[56] Giefers, H., Koval, S., Wortmann, G., Sturhahn, W., Alp, E.E., and Hu, M.Y., Phys Rev, B **74**, 094303 (2006).

[57] Tanis, E.A., Giefers, H., and Nicol, M.F., Rev. of Sci, Instrum. **79**, 023903 (2008).

[58] Mao, H.K., Bell, P.M., Shaner, J.W., and Steinberg, D.J. J. Appl. Phys., **49**, 3276 (1978).

[59] Mao, H.K., Xu, J., and Bell, P.M., J. Geophys. Res. **91**, 4673 (1986).

[60] Lipkin, H. J., Ann. Phys. **9**, 332 (1960).

[61] Johnson, D.W., and Spence, J.C.H., J. Phys. D: Appl. Phys. **7**, 62 (1974).

[62] Sturhahn, W., Hyperfine Interact. **125**, 149 (2000).

[63] Lipkin, H. J., Phys. Rev. B. **52**, 10073 (1995).

[64] Lubbers, R., Grüsteudel, H.F., Chumakov, A.I., and Wortman, G., Science **287**, 1250 (2000).

VITA

Graduate College
University of Nevada, Las Vegas

Elizabeth Anne Tanis

Degrees:
    Bachelor of Sciences, Physics, 2006
    California Lutheran University

Publications:
    E. Tanis, H. Giefers, M.F. Nicol, *Novel rhenium gasket design for nuclear resonant inelastic x-ray scattering at high pressure*, Rev. Sci. Inst. 79 (2008) 023903
    H. Giefers, E. Tanis, S.P. Rudin, C. Greeff, X. Ke, C. Chen, M.F. Nicol, M. Pravica, W. Pravica, J. Zhao, A. Alatas, M. Lerche, W. Sturhahn, and E. Alp, *Phonon Density of States of Metallic Sn at High Pressure*, Phys. Rev. Lett. 98 (2007) 245502.

Oral Presentations:
    Partial Phonon Density of States of Fe Solid Solutions by Nuclear Resonant Inelastic X-Ray Scattering Under High Pressure Western Regional Meeting of The American Chemical Society, September 25, 2008, Las Vegas, NV
    Phonon Density of States of Tin Under High Pressure Scientific Applications of Nuclear Resonant Scattering, May 8, 2008, Argonne National Laboratory, IL

Thesis Title:
    Partial Phonon Density of States of 57-Iron and 161-Dysprosium in $DyFe_3$ by Nuclear Resonant Inelastic X-Ray Scattering Under High Pressure

Thesis Examination Committee:
    Chairperson, Dr. Lon Spight
    Co-Chairperson, Dr. Dave Schiferl
    Committee Member, Dr. Pamela Burnley
    Committee Member, Dr. Len Zane
    Graduate Faculty Representative, Dr. Adam Simon